(Received 17 July 2024, Accepted 29 August 2024, Scheduled 13 September 2024)

A Dual Transmission Zero Bandpass Filter Employing Novel Hairpin-Coupled Resonators for Improved Stopband Characteristics Application the Vital Signs Detection Radar

Mingming Gao[1, 2], Yunshu Yang[2, *], Jingchang Nan[2], Handong Wu[3], Xiaolin Wang[3], and Xuanye Cui[3]

[1] *Ordos Institute of Liaoning Technical University, Ordos, China*
[2] *College of Electronic and Information Engineering, Liaoning Technical University, China*
[3] *Xi'an Hengda Microwave Technology Development Co., LTD, China*

ABSTRACT: Conventional hairpin band-pass filters (BPFs) typically have poor stopband performances. Therefore, this paper proposes a BPF with a center frequency of 24 GHz that employs a novel hairpin-coupled structure. An enhanced hairpin-coupled resonator topology is also introduced to improve the stopband suppression characteristics. Specifically, the proposed resonator and filter are configured through a hairpin structure and source-third resonator coupling, which afford a miniaturized size and coupling of the transmission zeros. Then, an equivalent circuit model is simulated to conduct loss analysis of the millimeter-wave (mm-wave) BPF, and the corresponding analytical parameters and result data are extracted. Furthermore, fast synthesis is achieved for the high stopband suppression mm-wave filter. The compact BPF developed is fabricated using quart glass process, with the corresponding measurements revealing that the insertion Loss (IL) is less than 4.5 dB, and the return loss (RL) exceeds 9 dB within the passband. Meanwhile, the stopband suppression at 20.6 GHz and 28.6 GHz can reach 43 dB and 35 dB, respectively. Those advanced performances demonstrate the promising prospect of the proposed filter for its application in biological radar life feature monitoring.

1. INTRODUCTION

In recent years, with the increasing demand for heart rate detection, millimeter wave radar noncontact vital sign detection technology has drawn extensive attention [1–5]. However, passive and active devices are strongly integral to the chip, with band-pass filters (BPFs) contributing to one of the most essential device parts [6]. In a wireless communication system, BPF averts interference signals from complicated surroundings. Expansive stopband suppression is crucial as it dramatically increases the mm-wave communication operation, which BPFs can realize. Commonly, a 24 GHz detection frequency of the window region is used.

Recently, with the increased application of millimeter wave technology, low-loss planar millimeter wave filters have become a research hotspot. Compared with the waveguide genre, hairpin-coupled microstrip line genre BPFs exist in circuit integration. In addition, the hairpin-coupled microstrip band-pass filter has strong virtues in frequency selection and frequency separation function and is widely used in radar, microwave communication, and other fields.

However, high stopband suppression is a big challenge for the performance of mm-wave filters. Many microstrip line BPFs work under low frequency, exhibiting weak stopband suppression and poor return loss within the passband. Furthermore, further chip packaging requires more mm-wave RF chips due to a complicated RF front-end structure. Thus, a valid setup for a traditional hairpin-coupled microstrip line band-pass filter is challenging. In addition, to achieve a wide stopband and high passband selectivity, a higher order of BPF is required, resulting in a poor IL.

Generally, a small circuit size and high stopband suppression lead to poor BPF filtering performance. Moreover, small circuit size and high stopband rejection are difficult to obtain simultaneously; thus, a trade-off during the design procedure is inevitable. Hence, this paper develops an improved hairpin-coupled structure for high stopband suppression BPF. Unlike conventional hairpin filters, capacitance and inductance parameters are given within the filter design circuit. A compact size and two transmission zeros (TZs) are generated to couple a source-third resonator.

The proposed filter places a band-pass filter forward in the 24 GHz center frequency with a 4.5 GHz bandwidth to monitor the biological radar. Based on the traditional hairpin-coupling filter, an improved circuit structure is proposed for the hairpin-coupled bandpass filter. For experimental verification, a high stopband suppression filter with a compact size is designed and fabricated using quart glass technology. Compared with existing literature, the proposed design reduces the area, increases the stopband attenuation, and improves the filter selectivity without accurately degrading the filter's performance, covering the K-band. The proposed band-pass filter can be applied in monitoring systems for biological radar life characteristics, significantly promoting circuit integration and system miniaturization [7, 8].

* Corresponding author: Yunshu Yang (yangyunshu@sylincom.com).

TABLE 1. Parameters of the seventh-order hairpin resonator.

Parameter	Value/mm	Parameter	Value/mm	Parameter	Value/mm
W_1	0.12	L_3	1.53	S_3	0.08
W_2	0.12	L_4	1.60	S_4	0.08
W_3	0.12	L_5	1.60	S_5	0.05
W_4	0.12	L_6	1.53	S_6	0.02
W_5	0.12	L_7	1.42	S_7	0.05
W_6	0.12	L_8	1.25	S_8	0.05
W_7	0.12	L_9	1.45	d_1	0.16
W_8	0.12	L_1	1.45	d_2	0.12
L_1	1.25	S_1	0.02	L_{11}	0.51
L_2	1.42	S_2	0.05		

2. OVERVIEW OF THE PROPOSED FILTER

When being used for BPFs, the hairpin-coupled resonator demonstrates sound isolation and broad bandwidth characteristics. A half-wavelength resonator is an appropriate structure to design, although it cannot restrain harmonics. Nevertheless, the hairpin filter is essential as it affords a super option and high stopband suppression. Meanwhile, strengthening a plan's filtering manifestation and theoretical knowledge can be fundamental.

Next, the filter circuit structure is presented, and then the hairpin structure of the mm-wave BPF is introduced and simulated. The proposed enhanced source-third resonator coupling topology will promote the stopband suppression characteristic. Furthermore, the lossy filter circuit structure is presented, and how it contributes to designing a high stopband suppression BPF is discussed. The improved hairpin-coupled microstrip band-pass filter comprises a resonator of the seventh order. Meanwhile, high selectivity and stopband suppression are realized using a source-third resonator and two TZs for good selectivity.

The magnetic coupling between the upper stopband and the source and the electric coupling between the lower stopband and the third stage resonator are both one-quarter wavelength ($\lambda/4$) in length. The length between the connecting two transmission lines is $(S_1+S_2+S_7+S_8+W_1+2*W_2+2*W_3+2*L_{11})$ mm. The parameters are listed in Table 1. According to the microwave transmission line theory, a one-half wavelength microstrip line with an open terminal is equivalent to a series resonant circuit. When the length of the transmission line is $\lambda/4$, the filter has the characteristics of bandpass filtering. In addition, the parallel coupled transmission line can use parity model analysis. Since this property produces transmission zero points, the length of the two improved transmission lines is $\lambda/4$ wavelength.

3. THE FILTER CIRCUIT MECHANISM FOR HAIRPIN BPF

Initially, the conventional and proposed structures of mm-wave hairpin BPF are provided, with its lossy equivalent circuit model allowing its analysis. This is important, as according to Section 1, the demanding specifications cause relevant problems for mm-wave BPFs.

3.1. Lossy Equivalent Circuit for Conventional Hairpin Resonator BPF

Hairpin band-pass filters have a compact structure, which can be theoretically obtained by parallel line coupling or a half-wavelength resonant structure unit bending into a "U" shape. This structure is called hairpin resonator, and its 3D model and equivalent circuit are illustrated in Fig. 1(a). From the microstrip theory, a half-wavelength series resonance circuit with two ends at the microstrip line is equivalent to two capacitors. The conventional hairpin integral circuit is depicted in Fig. 1(b).

Using full-wave electromagnetic (EM) simulation software [9], the initial capacitor and inductor can be acquired, which aligns with its equivalent circuit. Therefore, the circuit parameters, $C_{qj}(j = 1\ldots13)$, $L_{qj}(j = 1\ldots7)$ can be calculated as follows [10]:

$$L_{qj}\,|_{j=1\cdots n} = \frac{1}{\omega_0^2 C_b} \quad (n = 1\cdots7) \tag{1}$$

$$C_{qj}\,|_{j=1\cdots n} = \frac{1}{\omega_0^2 L_b} \quad (n = 1\cdots7) \tag{2}$$

$$C_{qj}\,|_{j=8\cdots n} = \frac{1}{\omega_0^2 L_{qj}} \quad (n = 8\cdots13) \tag{3}$$

$$K_{j,j+1}\,|_{j=1\cdots n-1} = \frac{w\omega_0}{\omega_1'}\sqrt{\frac{L_{qj}L_{qj+1}}{g_j g_{j+1}}} \tag{4}$$

$$M_{j,j+1}\,|_{j=1\cdots n-1} = \frac{K_{j,j+1}}{\omega_0} \tag{5}$$

$$w = \frac{\omega_2 - \omega_1}{\omega_0} \tag{6}$$

where C_b and L_b are the normalized capacitors and inductors of the low-pass filter circuit; $K_{j,j+1}$ is the K-inverter; $M_{j,j+1}$ denotes the mutual coupling parameters; w is the fractional bandwidth; ω_0 is the passband center frequency; and ω_1 and

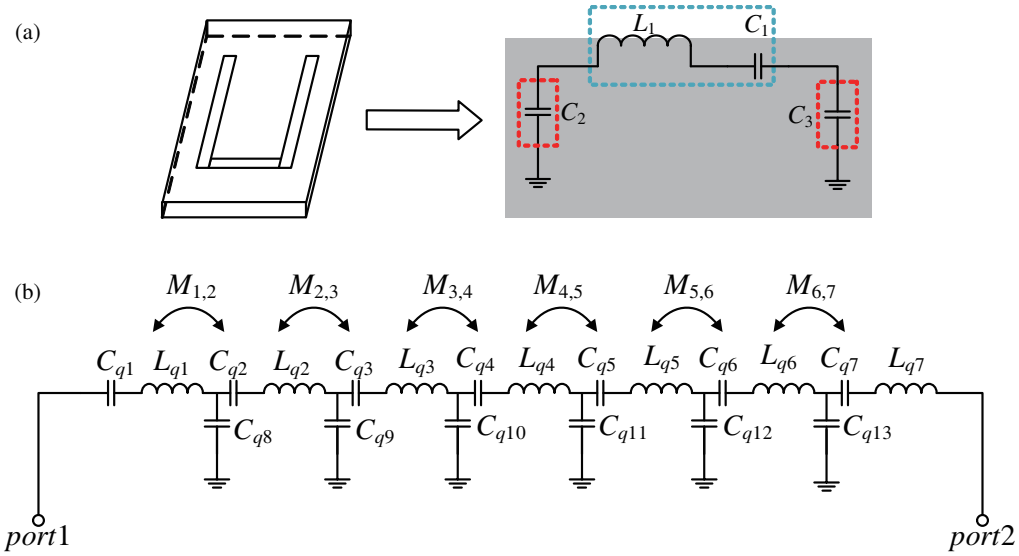

FIGURE 1. Hairpin resonator and conventional hairpin filter. (a) Hairpin resonator 3D model and equivalent circuit. (b) Traditional filter of the hairpin circuit.

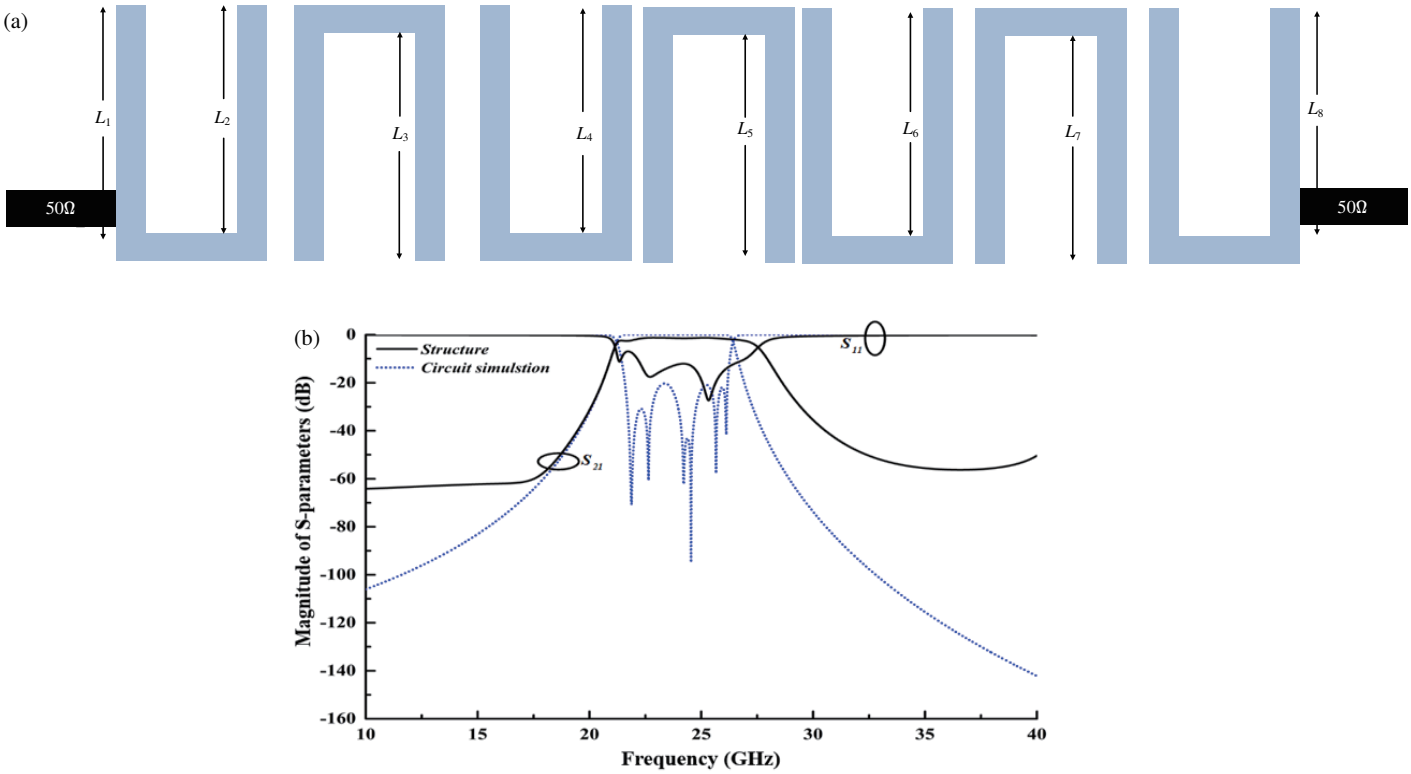

FIGURE 2. Conventional seventh-order hairpin resonator. (a) Structure. (b) Structure and circuit simulation of the filter.

ω_2 are the upper and lower sideband frequencies. Moreover, g_0, g_1, g_j, and g_{j+1} are low-pass archetype filter elements. Fig. 2(a) presents the structure of the conventional hairpin filter. Fig. 2(b) presents the S-parameters of the traditional hairpin filter using the EM software simulator. Table 2 reports the capacitance and inductance parameters, calculated using Eqs. (1)–(6), which exploit the Advanced Design System (ADS).

3.2. Lossy Equivalent Circuit for Improved Hairpin Resonator BPF

The proposed BPF circuit illustrated in Fig. 3 aims to improve stopband suppression. It comprises seven hairpin resonators, a source-third resonator, and two feeding lines. $E_{3,new}$ in Fig. 3 represents the electric coupling to the third resonator, and

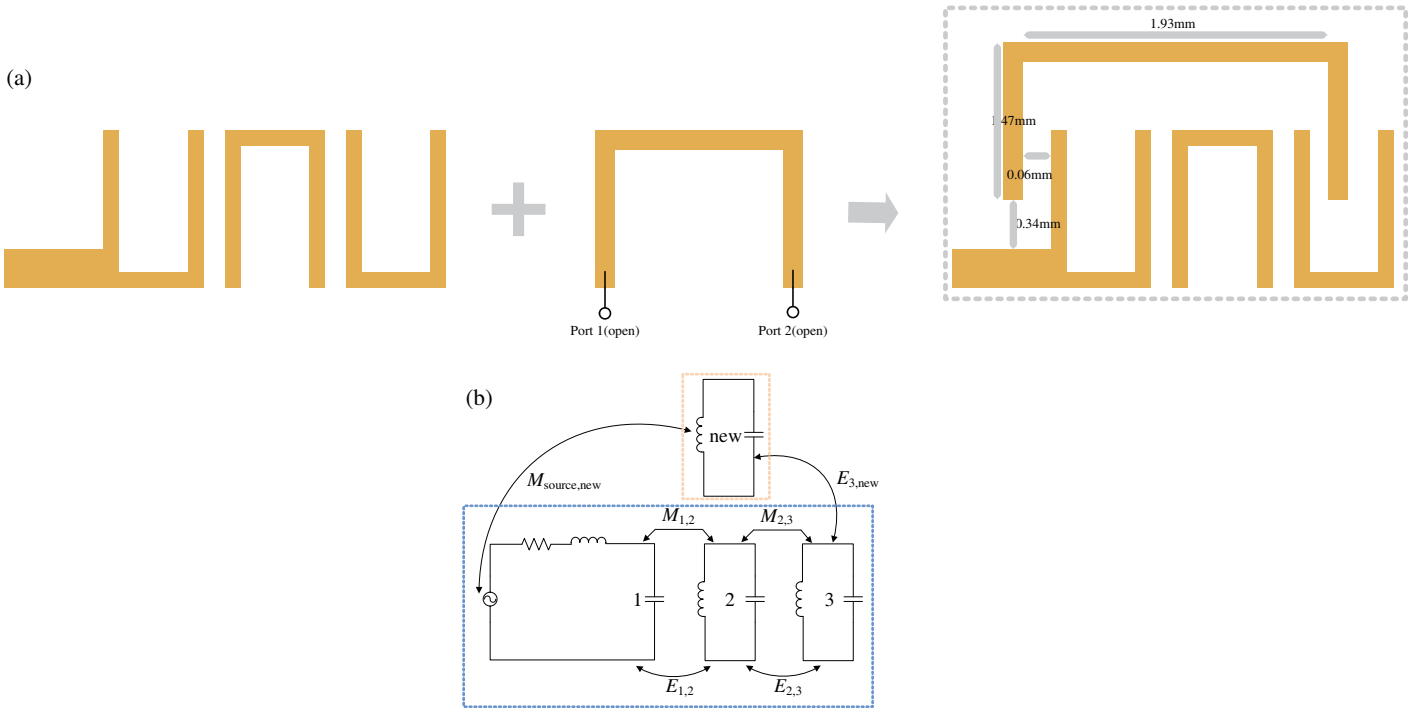

FIGURE 3. Improved structure and circuit interdigital. (a) Schematic layouts. (b) Lossy equivalent mechanism.

TABLE 2. Extracted circuit parameters for the hairpin resonator.

Parameter	Performance	Parameter	Performance
C_{q1}	37.96 fF	C_{q11}	281.2 fF
C_{q2}	44.46 fF	C_{q12}	259.6 fF
C_{q3}	40.59 fF	C_{q13}	175.3 fF
C_{q4}	40.41 fF	L_{q1}	1.409 nH
C_{q5}	40.59 fF	L_{q2}	1.409 nH
C_{q6}	4.46 fF	L_{q3}	1.409 nH
C_{q7}	37.96 fF	L_{q4}	1.409 nH
C_{q8}	175.3 fF	L_{q5}	1.409 nH
C_{q9}	259.6 fF	L_{q6}	1.409 nH
C_{q10}	281.2 fF	L_{q7}	1.409 nH

$M_{source,new}$ is the magnetic coupling to the source. Fig. 3(a) reveals that two terminals of the microstrip wire are equivalent to capacitive ground. Thus, the hybrid electromagnetic coupling [11] structure of the improved hairpin resonator structure is utilized, as depicted in Fig. 3(b). The simulation parameters of the proposed BPF are calculated using the Advanced Design System (ADS). Fig. 4 demonstrates that a favorable response is perceived, certifying the practicality of the proposed hybrid electromagnetic coupling circuit mechanism.

Due to the hairpin resonator, the BPF is realized through an applicable coupling structure. As depicted in Fig. 4(a), the mixed electric and magnetic coupling is generated between the source and the third resonator, represented by an electric coupling to the source and the magnetic coupling to the third resonator (Fig. 4(b)). Consequently, the S-parameters of the filter structure and lossy circuit mechanism can be calculated (Fig. 4(c)).

As discussed, an excellent S-parameter response can be realized within the band of $10 \sim 40$ GHz, thereby generating precisely two stopband TZs. In this study, the two TZs produced consider the electric and magnetic coupling impact between the source and the third resonator. To summarize, unmatched EM and circuit simulations are obtained within the out-of-band region, as illustrated in Fig. 4(c). Therefore, the proposed hairpin circuit improves the stopband suppression of the enhanced hairpin resonator filter.

3.3. Two TZs Based on Circuit Analysis

The improved filter circuit overcomes the challenge of low stopband suppression for the new-coupled BPF. Indeed, initially, high suppression is achieved by adding TZs. According to Fig. 4, the filter circuit model of the improved hairpin filter is simulated, and its stopband suppression can be used for various capacitance and inductance values of the new-couple resonator. The stopband suppression augments fast with larger capacitance and inductance parameters, particularly the capacitance parameters. Besides the resonators, selecting a high-selectivity coupling topology is also crucial. Similarly, the hairpin resonator remains unchanged, with fixed capacitance and inductance parameters. Good impedance matching is achieved by appropriately modulating the inter-resonator coupling and the coupling between the source and the third resonator.

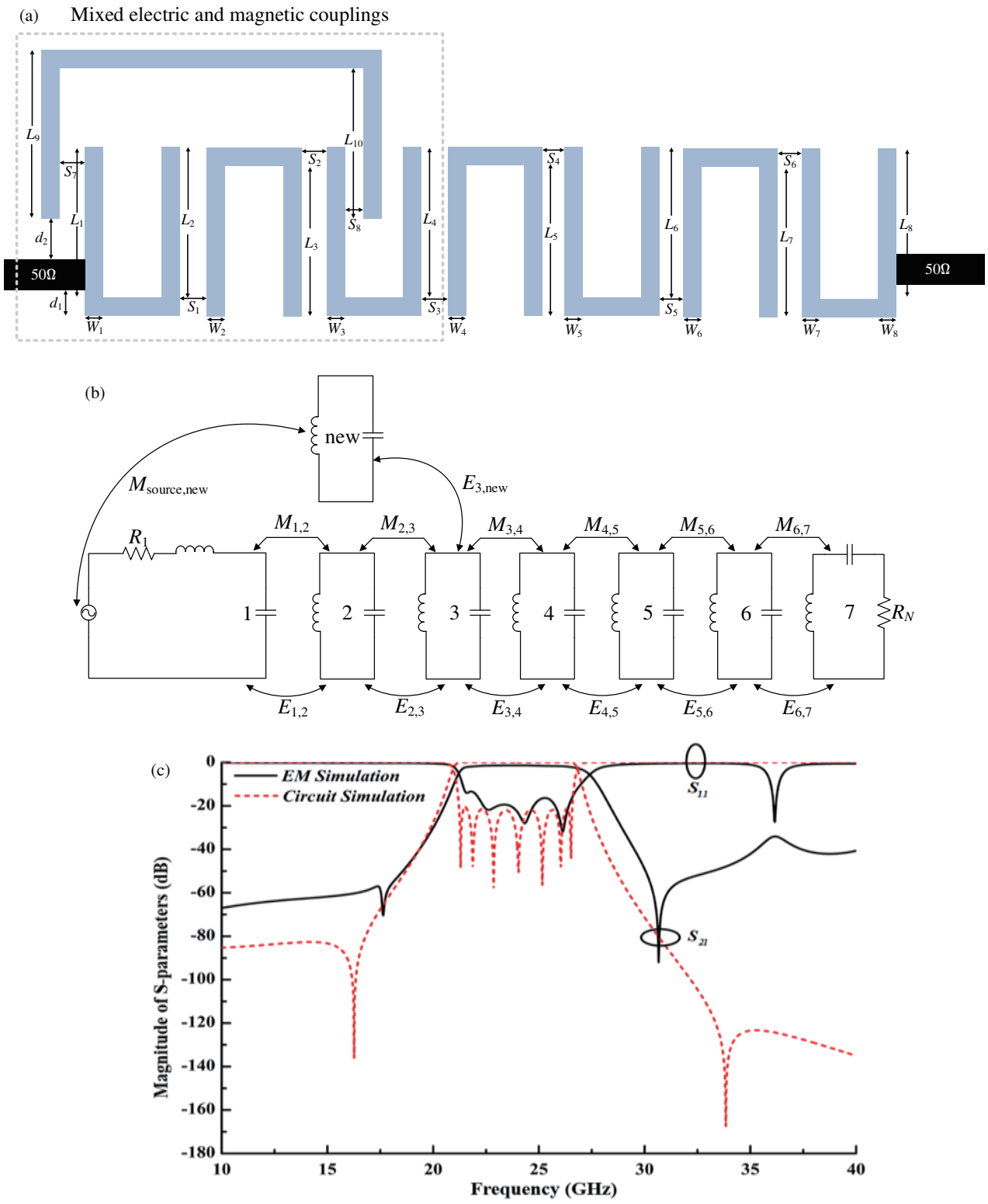

FIGURE 4. Seventh-order hairpin BPF using source-third resonator couple. (a) Proposed structure of the BPF. (b) The equivalent filter circuit mechanism. (c) EM physical structure and circuit calculations.

4. DESIGN OF TWO TZS NEW-COUPLED HAIRPIN BPF

Based on the above analysis, this section designs, fabricates, and measures a 24 GHz BPF with two TZs.

4.1. Hairpin Resonator Design

The length of a transmission line connected to the load at one end and the input impedance at the other is $\lambda/2$, where λ is the wavelength. Moreover, the reciprocal impedance between

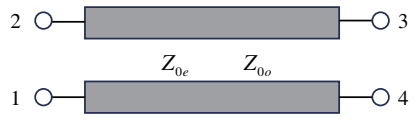

FIGURE 5. Coupling unit.

the coupled transmission lines exists in semblable characteristics. The improved filter conforms with the odd-even mode impedance analysis, which generates transmission zero points. As illustrated in Fig. 5, it comprises a coupled transmission line segment. The voltage equation is:

$$\begin{bmatrix} v_{\mathrm{I}} \\ v_{\mathrm{II}} \end{bmatrix} = \begin{bmatrix} z_{\mathrm{II}} & z_{\mathrm{III}} \\ z_{\mathrm{III}} & z_{\mathrm{IIII}} \end{bmatrix} \begin{bmatrix} i_{\mathrm{I}} \\ i_{\mathrm{II}} \end{bmatrix} \tag{7}$$

In addition,

$$\begin{aligned} [v_{\mathrm{I}}] &= \begin{bmatrix} v_1 & v_2 \end{bmatrix}^t, \quad [v_{\Pi}] = \begin{bmatrix} v_3 & v_4 \end{bmatrix}^t \\ [z_{\mathrm{III}}] &= \begin{bmatrix} z_{31} & z_{32} \\ z_{41} & z_{42} \end{bmatrix}, \quad [z_{\Pi\Pi}] = \begin{bmatrix} z_{33} & z_{34} \\ z_{43} & z_{44} \end{bmatrix} \end{aligned} \tag{8}$$

When ports 3 and 4 are loaded, the impedance matrix of the novel ports 1 to 2 is:

$$[Z] = [z_{\mathrm{II}}] + Y_L [z_{\mathrm{III}}] ([U] - Y_L [z_{\Pi\Pi}])^{-1} [z_{\mathrm{II}}] \tag{9}$$

where $[U]$ is a 2×2 identity matrix. Provided that ports 3 and 4 are open, the self-impedance and mutual impedance of ports 1 to 2 are derived as follows:

$$\begin{aligned} Z_{11} = z_{11} = -\frac{j}{2}(Z_{0e} + Z_{0o}) \cot\theta \\ Z_{12} = z_{12} = -\frac{j}{2}(Z_{0e} - Z_{0o}) \cot\theta \end{aligned} \tag{10}$$

where $\theta = \beta l$ and $\beta = \omega\sqrt{\mu\varepsilon}$ represent the propagation constant, coupled with the length of the branch, acquired from the impedance specification Z_e and Z_o which are on behalf of the impedance in odd and even modes, respectively.

Figure 6(a) illustrates the equivalent circuit of a second-order band-pass filter with equal resistance parameters $R_1 = R_2 = R$ at the source and load ends. Assuming that the frequency change reactance $M(\omega)$ represents the coupling between the resonators, the voltage loop equation in Fig. 6(b) is [12]:

$$\begin{bmatrix} e_s \\ 0 \end{bmatrix} = \begin{bmatrix} R + \omega_0 L \cdot p & -jM(\omega) \\ -jM(\omega) & R + \omega_0 L \cdot p \end{bmatrix} \cdot \begin{bmatrix} i_1 \\ i_2 \end{bmatrix} \tag{11}$$

In addition,

$$p = j\left(\frac{\omega}{\omega_0} - \frac{\omega_0}{\omega}\right) \tag{12}$$

When the electric and magnetic coupling quantities in couplings are approximately similar, the coupling reactance $M(\omega)$ should be reflected simultaneously, given these two types of coupling. Therefore, the electric and magnetic couplings can be expressed in the form of reactance:

$$M(\omega) = \omega L_m - \frac{1}{\omega C_m} = \omega_m L_m \left(\frac{\omega^2 - \omega_m^2}{\omega\omega_m}\right) \tag{13}$$

where L_m and C_m are the coupling inductance and capacitance, respectively.

When the reference planes A-A and B-B can be opened,

$$C_1 = (C \cdot C_m)/(C_m - C) C_2 = C_m/2 \tag{14}$$

If electric and the magnetic walls are inserted on the symmetric plane T-T,

$$L_{odd} = L - L_m L_{even} = L + L_m \tag{15}$$

Converting it to the odd mode frequency provides:

$$\omega_{odd} = \sqrt{\frac{1}{L_{odd} \cdot C_{odd}}} = \sqrt{\frac{C_m - C}{(L - L_m) \cdot C \cdot C_m}}$$

(odd-mode) (16)

$$\omega_{even} = \sqrt{\frac{1}{L_{even} \cdot C_{even}}} = \sqrt{\frac{C_m + C}{(L + L_m) \cdot C \cdot C_m}}$$

((even-mode) (17)

Dividing Eq. (13) by $\omega_0 L$ yields:

$$\begin{aligned} k &= \frac{M(\omega_0)}{\omega_0 L} = \frac{\omega_0 L_m - 1/\omega_0 C_m}{\omega_0 L} \\ &= \frac{K_M}{\omega_0 L_0} - \frac{K_E}{\omega_0 L_0} = \frac{L_m}{L_0} - \frac{C_0}{C_m} = M_C - E_C \end{aligned} \tag{18}$$

where E_C is the electric coupling coefficient, and M_C is the magnetic coupling coefficient. The extraction formula of the electromagnetic coupling coefficient is derived from Eqs. (16), (17), and (18):

$$E_C = \frac{\omega_m^2(\omega_{odd}^2 - \omega_{even}^2)}{2\omega_{odd}^2\omega_{even}^2 - \omega_m^2(\omega_{odd}^2 + \omega_{even}^2)} \tag{19}$$

$$M_C = \frac{\omega_{odd}^2 - \omega_{even}^2}{\omega_{odd}^2 + \omega_{even}^2 - 2\omega_m^2} \tag{20}$$

From Eqs. (18), (19), and (20), it is evident that when the electrical coupling coefficient $E_C = 0$, $C_m = \infty$,

$$k = M_C - E_C = M_C = \frac{\omega_{odd}^2 - \omega_{even}^2}{\omega_{odd}^2 + \omega_{even}^2},$$

when $E_C = 0$ (21)

When the magnetic coupling coefficient $M_C = 0$, $L_m = 0$,

$$k = M_C - E_C = -E_C = \frac{\omega_{odd}^2 - \omega_{even}^2}{\omega_{odd}^2 + \omega_{even}^2},$$

when $M_C = 0$ (22)

From the electromagnetic coupling coefficient,

$$\frac{M_C}{E_C} = \frac{L_m/L}{C/C_m} = \frac{L_m C_m}{LC} = \frac{\omega_0^2}{\omega_m^2} \tag{23}$$

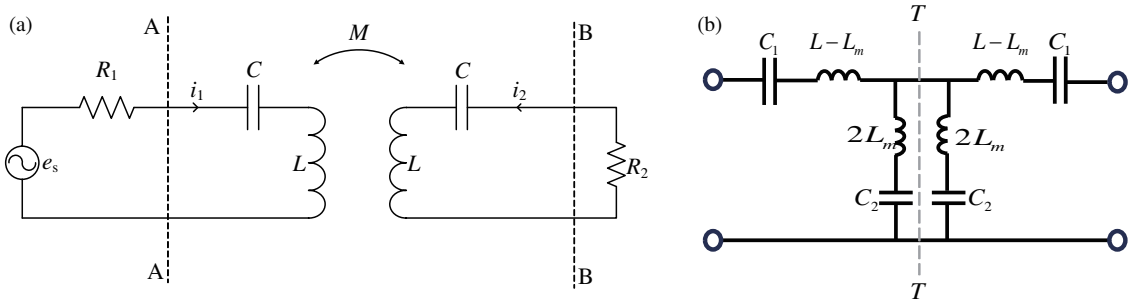

FIGURE 6. Second-order order bandpass filter circuit. (a) Equivalent circuit of a second-order bandpass filter with frequency-varying coupling $M(\omega)$; (b) Reference surface A-A and B-B open circuit equivalent circuit.

4.2. Two TZs Coupling Topology for Hairpin BPF

The electric and magnetic coupling coefficients can be acquired between the improved resonator structure and the source-third resonator. Eqs. (11)–(23) account for the improved hairpin band-pass filter generating transmission zero in the upper and lower stopbands, thus improving the filter's stopband suppression. The TZ of the upper stopband can be generated using the magnetic coupling between the proposed structure and the source. Accordingly, the magnetic coupling coefficient is calculated from Eqs. (14)–(20). The TZ of the lower stopband can be produced through the electric coupling between the proposed structure and the third-stage resonator. The electrical coupling coefficient is calculated from Eqs. (14)–(19).

In line with Section 3, the stopband suppression of hairpin BPF is increased by choosing a proper coupling method. The coupled structure is illustrated in Fig. 7(a), where S and L represent the source and load of the filter, respectively. As illustrated in Fig. 7(b), the external coupling is modulated through the coupling gap S_4. Meanwhile, external coupling hinges on the source-third resonator, which can generate two TZs. Notations 1 to 7 indicate the hairpin resonator, and the S-parameters can be simulated by appropriately choosing a different combination of d_2 and L_9, as shown in Fig. 7(c). As illustrated, the stopband suppression points are located at 17.64 GHz and 30.66 GHz, which reach 70.4 dB and 91.9 dB, respectively. Therefore, higher stopband suppression is generated by choosing the appropriate coupling structure of the newly-coupled hairpin BPF. Fig. 7(d) compares the improved and traditional S parameters. It was found that the conventional hairpin-coupled structure could only suppress -40 dB at 30.66 GHz, and no TZs were generated. Besides, the coupled mode for the source-third resonator has been varied to create TZs on the stopband response. In response, the filter generated TZs and produced return loss (RL) within the passband. Thus, we investigate a source-third resonator structure to improve the stopband.

The influence of S and L on the passband is also simulated and analyzed. It is found that L_4 is the most influential parameter, with Fig. 8 revealing the frequency transforms of the filter with diverse L_4. Fig. 8(a) highlights that by increasing L_4, the passband shifts to a lower frequency. Fig. 8(b) presents the influence of S_4. By increasing S_4, the bandwidth of the filter is broadened accordingly. Fig. 8(c) illustrates the impact of d_2. By increasing d_2, the lower barrier band TZ moves to a high frequency.

To avoid cavity resonance of higher-order LSM, the width of the rectangular cavity of band-pass filters in K-band segments is designed to be 5 and 1.7 mm, respectively. Furthermore, the E-plane waveguide-to-microstrip line transition mechanism [13–17] was accommodated by coupling the energy to the microstrip line from the rectangular waveguide. The waveguide-to-microstrip structure is depicted in Figs. 9(a) and (b).

4.3. Implementation of Two TZs Hairpin BPF

Based on the analysis of the filter circuit structure and TZs, the design flow of an mm-wave high stopband suppression newly-coupled hairpin BPF can be summarized as follows:

1) Process 1: Obtain the circuit parameters (C_{qn} ($n = 1 \ldots 13$), L_{qn} ($n = 1 \ldots 7$)) following the design criteria of the initial hairpin BPF using ADS.

2) Process 2: Calculate the initial electrical and magnetic coupling coefficients based on the empirical Eqs. (7)–(23).

3) Process 3: Calculate the coupled resonator.

4) Process 4: Calculate the new-coupled hairpin BPF in HFSS.

5) Process 5: Optimize the hybrid electromagnetic coupling parameters obtained in step 4.

6) Process 6: Duplicate steps 2–5 to the indicator requirements are demanded.

7) Process 7: Acquire the ultimate structure and physical parameters for the hairpin BPF.

According to the design process, a hairpin BPF with two TZs are established spelling out vital signs detection radar, whose filter indicators can be designed as follows:

1) f_0: 24 GHz

2) BW: 4.5 GHz

3) RL: > 20 dB

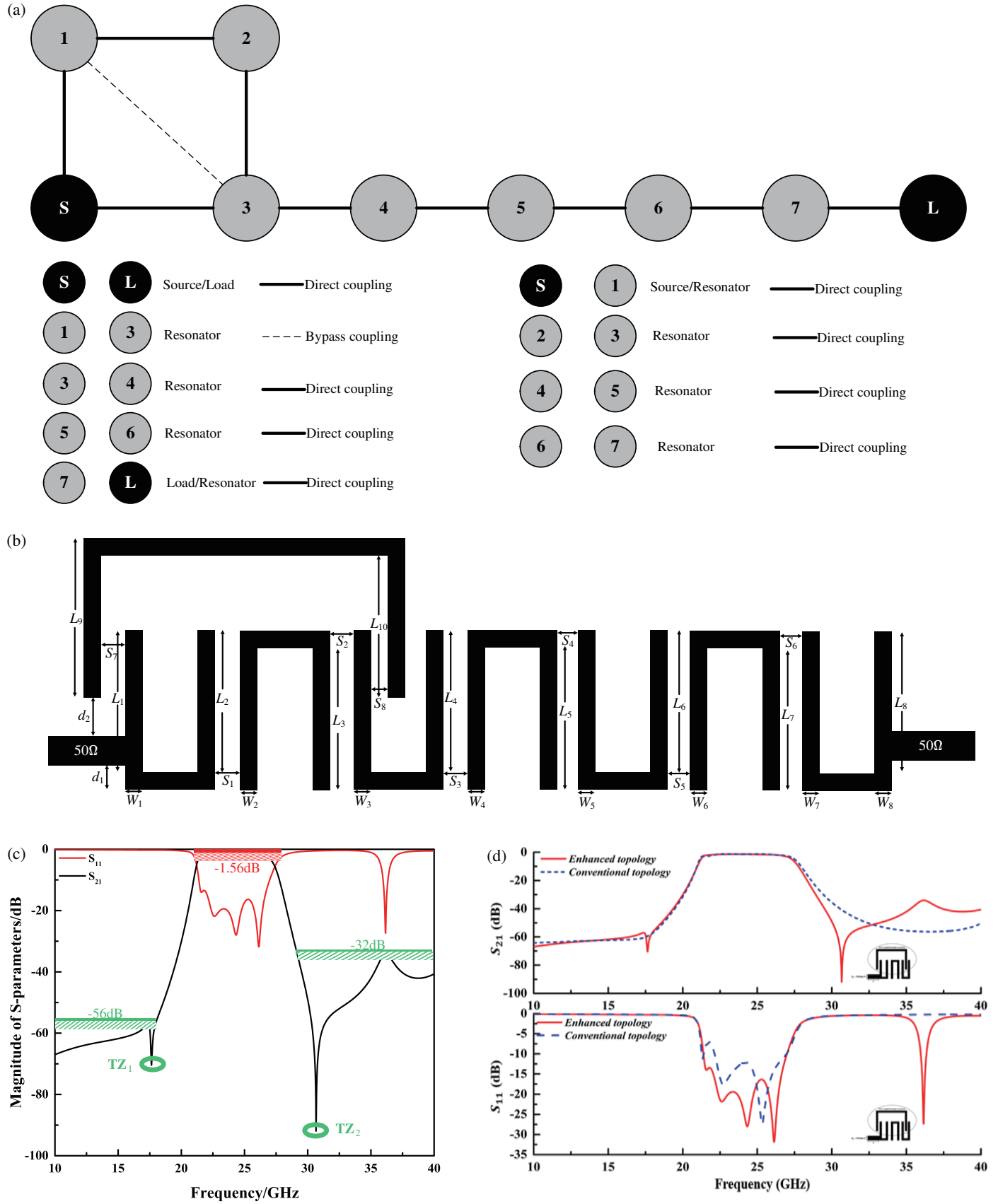

FIGURE 7. Proposed dual TZ high stopband suppression hairpin BPF. (a) Theoretical coupling. (b) Schematic layout. (c) Simulated responses of dimensions. (d) Improvement over the traditional S parameters calculation.

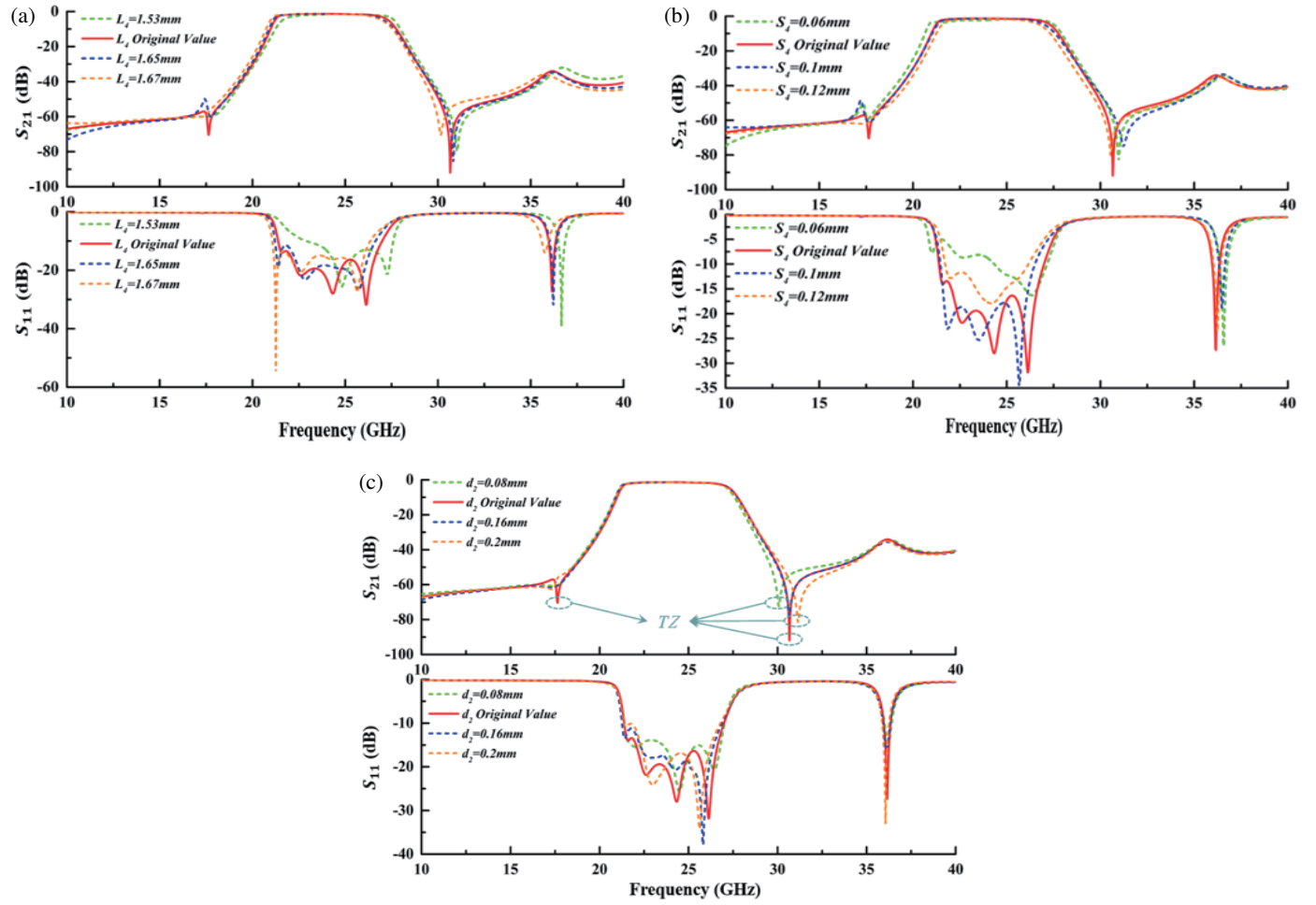

FIGURE 8. Variations when L_4, S_4, d_2 increase. (a) Calculated results of BPFs with tuned L_4. (b) Calculated results of BPFs with tuned S_4. (c) Calculated results of BPFs with tuned d_2.

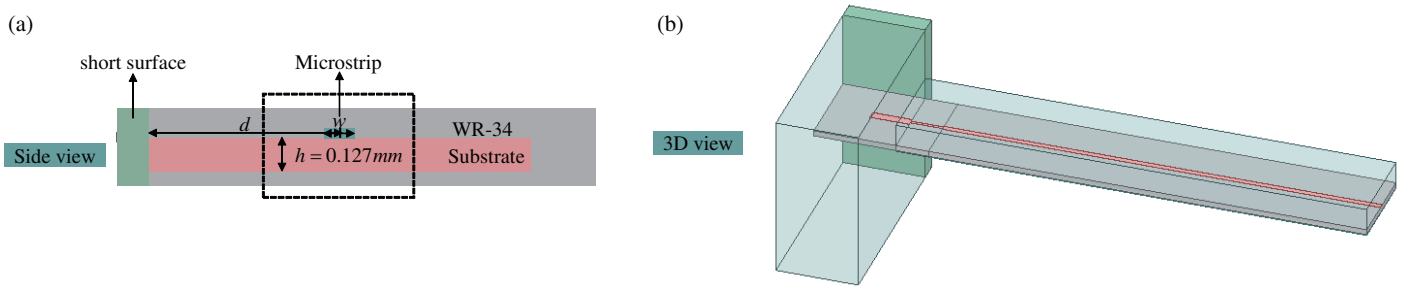

FIGURE 9. Waveguide-to-microstrip transition. (a) Side view. (b) 3D view.

4) IL: < 2 dB

5) Stopband attenuation: @30 GHz $>$ 40 dB; @18 GHz $>$ 40 dB

4.4. Discussion

This study designs and fabricates a microstrip-type bandpass filter using a 0.127 mm thick quartz-glass substrate with an interrelated dielectric constant of 3.78. The quartz glass is connected to the cavity by conductive silver. The machinable model is mounted in a rectangular cavity. Figs. 10(a), (b), and (c) depict patterns of the BPF module and its circuit.

Besides, the physical parameters of the designed filter are obtained, and the Agilent E8364B network analyzer is used to measure our filter's technical specifications, as illustrated in Fig. 11. The measured nuclear frequency is 24 GHz with a passband from 22.8 to 25.2 GHz, and the measured IL is 4.5 dB within the passband. Additionally, two TZs are located at 20.6

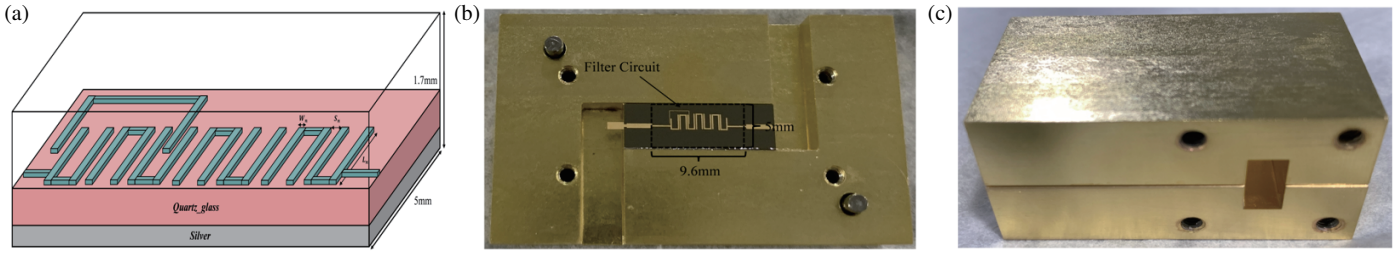

FIGURE 10. Proposed source-third resonator BPFs with the waveguide-to-microstrip transition. (a) 3D model. (b) Waveguide test model. (c) Cavity structure.

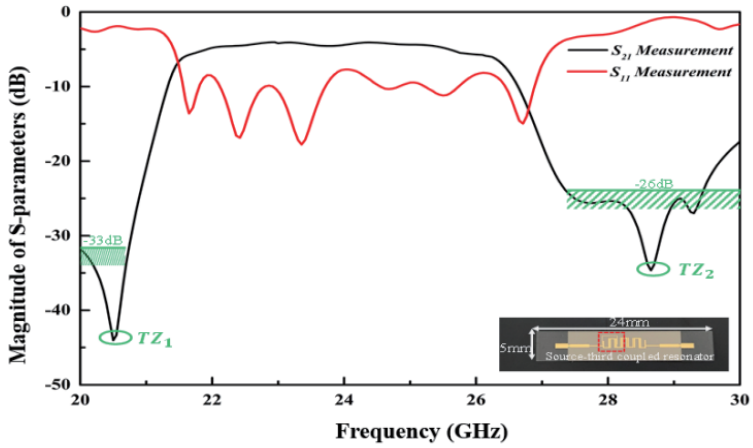

FIGURE 11. Measured response of the proposed source-third coupled resonator.

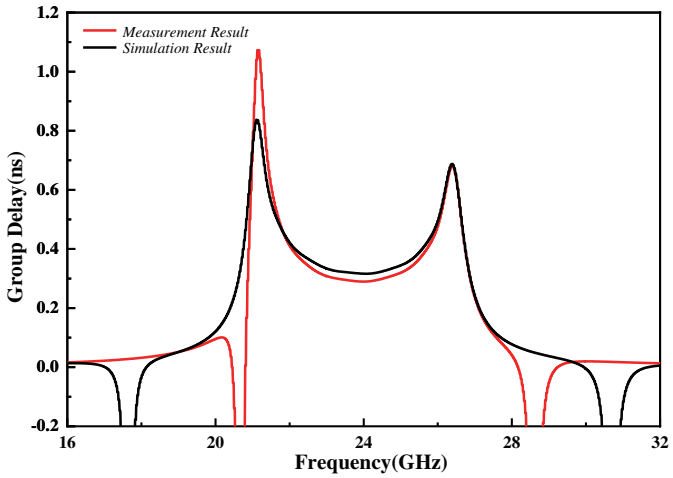

FIGURE 12. Measured and simulated responses of the proposed source-third coupled resonator.

and 28.6 GHz, reaching 43 dB and 35 dB, respectively. Fig. 12 illustrates the group delay results of the simulated and measured filters. The passband's group delay variation (GDV) is ± 0.8 ns, which is very small. Thus, it is faster than the previously published papers.

Regarding the insertion loss and slope characteristics outside the passband, the stopband suppression of the Chebyshev function at 18 GHz is about 60 dB, and the stopband suppression of the Elliptic function at 18 GHz is about 112 dB. Hence, the stopband suppression of the Elliptical function form filter is much higher than that of the Chebyshev filter under the same parameters, and the transition zero is steeper. Therefore, we adopt the Elliptic function form for filters with high stopband rejection requirements. The hairpin resonator can be further improved by using a ring-coupled filter in the form of an Elliptic function to enhance stopband rejection without introducing additional transmission zeros. At the same time, the greater the order is, the greater the insertion loss is, and the number of resonators can be appropriately reduced to ensure stopband suppression requirements.

The center frequency corresponds to the desired frequency of 24 GHz. The return loss was at 9 dB, which was not in accordance with the specification, i.e., ≥ 10 dB. Hence, this performance is poor. The insertion loss was also 4.5 dB, which was lower than the specification of ≤ 3 dB. Thus, the insertion loss value was not in accordance with the specification. The difference between the electromagnetic simulation and the measurement results is due to the following reasons: 1. The thickness of the quartz glass substrate made by the manufacturer of the filter board is biased. 2. During the measurements, the waveguide production is not integrated but is divided into two modules for assembly. Thus, as the application frequency increases, the impact on the performance of the waveguide becomes more significant. 3. When designing the microstrip-waveguide transition,

TABLE 3. Extracted circuit parameters for hairpin resonator - A comparison between the proposed hairpin-coupled microstrip BPFs and previously published designs.

Reference	f_0/(GHz)	FBW (%)	RL (dB)	IL (dB)	TZs Num	Group Delay (ns)	size (λ_g^2)
[18]	10–11.2	1.13	> 10	< 2.65	0	NA	0.38×0.28
[19]	4.42/7.2	2.1/0.1	$> 17.56/17.9$	$< 0.5/0.86$	0	$< 2.4/2.2$	0.23×0.11
[20]	5.7/6.5	3.66/2.33	$> 35/30$	NA	0	$< 1.6/2.5$	0.22×0.11
[21]	1.57/2.38	9.9/6.5	NA	$< 1.21/1.95$	2	$< 10/11$	NA
[22]	2.45/5.2	7.7/7.1	$> 10/20$	$< 1.4/1.2$	1	3.5/2.2	0.15×0.09
[23]	2.45/5	NA	NA	$< 2.2/1.6$	2	NA	0.18×0.2
[24]	9.3	3	> 19	< 3.7	0	NA	0.08×0.11
This work	24	18.75	> 9	< 4.5	2	< 1.1	0.032×0.058

the impedance transformation is biased. The above-mentioned reasons lead to a nonuniform electromagnetic field energy distribution that affects the filter's selectivity.

Additionally, dielectric loss and conductor loss significantly influence the insertion loss, return loss, and transmission efficiency of the filter. Even if the selected dielectric material has a low dielectric loss, energy loss is inevitable at higher frequencies. Therefore, the filter's insertion loss is increased by various factors, and the return loss is inevitably reduced.

Table 3 reports the contrasting results between the proposed filter and the reference design. Notably, all BPFs for MMW frequencies have a waveguide configuration, and all microstrip linear BPFs are designed for low-stopband suppression applications. Unlike the existing band-pass filters, the proposed hairpin BPF performs well with a high stopband suppression enough to be used at millimeter wave radar frequencies.

A vital sign radar sends radio waves to the body through noncontact means and analyzes the reflected signals to monitor the body's heartbeat and breathing. Given that newborns require good protection, the new technology radar can be used to locate and monitor infants, where the vital signs monitoring radar can monitor the breathing rate and heartbeat of the infants in cribs. During the detection, the heartbeat of the infants cannot be determined during the test due to the signal instability in the system. Therefore, filters must discard unnecessary signals. The front end of the monitoring radar comprises a transmitting antenna and two receiving antennas, and a band-pass filter and ground floor are placed on each antenna feeder. Therefore, a mm-wave filter with high stopband suppression is proposed to overcome the problem of signal instability in vital signs monitoring radar systems.

5. CONCLUSION

This article designs a high stopband suppressed BPF using a source-third resonator for monitoring biological radar life features. The proposed BPF using lossy filter circuit modeling is presented based on theoretical analysis. Furthermore, this article delves into the enhanced source-third coupling resonator topology to achieve a high stopband suppression. For experimental corroboration, the BPF is designed with an IL of 4.5 dB, 20.6 GHz, and 28.6 GHz stopband suppression, reaching about 43 dB and 35 dB, which are simultaneously obtained. The spurious suppression can be enhanced by utilizing a source-third coupled structure, and a wide rejection band can be obtained. In addition, a 40% size reduction and 18.75% relative bandwidth are realized for the BPF. High stopband suppression, high selectivity, and miniaturization can be achieved, demonstrating the improved hairpin BPF as an appealing candidate for vital signs detection radar.

ACKNOWLEDGEMENT

This work was supported by the University-local government scientific and technical cooperation cultivation project of Ordos Institute-LNTU (YJY-XD-2024-B-009), the Basic Scientific Research Project of the Education Department of Liaoning Province (JYTMS20230818), and the Applied Basic Research of Liaoning Province (2022JH2/101300275).

REFERENCES

[1] Petrović, V. L., M. M. Janković, A. V. Lupšić, V. R. Mihajlović, and J. S. Popović-Božović, "High-accuracy real-time monitoring of heart rate variability using 24 GHz continuous-wave Doppler radar," *IEEE Access*, Vol. 7, 74 721–74 733, 2019.

[2] Wang, J. and C. Li, "A human tracking and physiological monitoring FSK technology for single senior at home care," in *2018 40th Annual International Conference of the IEEE Engineering in Medicine and Biology Society (EMBC)*, 4432–4435, 2018.

[3] Sakamoto, T., "Noncontact measurement of human vital signs during sleep using low-power millimeter-wave ultrawideband MIMO array radar," in *2019 IEEE MTT-S International Microwave Biomedical Conference (IMBioC)*, Vol. 1, 1–4, Nanjing, China, May 2019.

[4] Shang, H., X. Zhang, Y. Ma, Z. Li, and C. Jin, "Random body movement cancellation method for FMCW radar vital sign detection," in *2019 IEEE International Conference on Signal, Information and Data Processing (ICSIDP)*, 1–4, Chongqing, China, Dec. 2019.

[5] Dong, Z., M. Zhang, J. Sun, T. Cao, R. Liu, Q. Wang, *et al.*, "A fatigue driving detection method based on frequency modulated continuous wave radar," in *2021 IEEE International Conference on Consumer Electronics and Computer Engineering (ICCECE)*, 670–675, Guangzhou, China, Jan. 2021.

[6] Weir, W. B., "Automatic measurement system for a multichannel digitally tuned bandpass filter," *IEEE Transactions on Instrumentation and Measurement*, Vol. 23, No. 2, 140–148, 1974.

[7] Nosrati, M. and N. Tavassolian, "Accurate doppler radar-based cardiopulmonary sensing using chest-wall acceleration," *IEEE Journal of Electromagnetics, RF and Microwaves in Medicine and Biology*, Vol. 3, No. 1, 41–47, 2019.

[8] Tedesco, S., J. Barton, and B. O'Flynn, "A review of activity trackers for senior citizens: Research perspectives, commercial landscape and the role of the insurance industry," *Sensors*, Vol. 17, No. 6, 1277, 2017.

[9] Chiu, H.-J., T.-F. Pan, C.-J. Yao, and Y.-K. Lo, "Automatic EMI measurement and filter design system for telecom power supplies," *IEEE Transactions on Instrumentation and Measurement*, Vol. 56, No. 6, 2254–2261, 2007.

[10] Sarma, G. R. and J. P. Barranger, "Capacitance-type blade-tip clearance measurement system using a dual amplifier with ramp/DC inputs and integration," *IEEE Transactions on Instrumentation and Measurement*, Vol. 41, No. 5, 674–678, 1992.

[11] Danisi, A., A. Masi, R. Losito, and Y. Perriard, "Electromagnetic analysis and validation of an ironless inductive position sensor," *IEEE Transactions on Instrumentation and Measurement*, Vol. 62, No. 5, 1267–1275, 2013.

[12] Southwick, R. A. and W. C. Dolle, "Line impedance measuring instrumentation utilizing current probe coupling," *IEEE Transactions on Electromagnetic Compatibility*, No. 4, 31–36, 1971.

[13] Xiao, Y., L. Ye, G. Cai, and Q. H. Liu, "A full Ka-band half height waveguide to microstrip transition," in *2015 Asia-Pacific Microwave Conference (APMC)*, Vol. 1, 1–3, Nanjing, China, Dec. 2015.

[14] Xu, J., T. Ye, D. Y. Pu, and M. Y. Wang, "A rectangular waveguide-microstrip transition based on the principle of magnetic coupling for millimeter-wave," in *2009 International Conference on Microwave Technology and Computational Electromagnetics (ICMTCE 2009)*, Beijing, China, Nov. 2009.

[15] Tuan, N. T., K. Sakakibara, and N. Kikuma, "Bandwidth extension of planar microstrip-to-waveguide transition by via-hole arrangement," in *2018 International Symposium on Antennas and Propagation (ISAP)*, 1–2, 2018.

[16] Tomar, S., S. K. Singh, L. Suthar, *et al.*, "E-plane waveguide to microstrip transition for millimeter wave applications," in *ICMARS 2010*, Dec. 2010.

[17] McClanahan, A., S. Kharkovsky, A. R. Maxon, R. Zoughi, and D. D. Palmer, "Depth evaluation of shallow surface cracks in metals using rectangular waveguides at millimeter-wave frequencies," *IEEE Transactions on Instrumentation and Measurement*, Vol. 59, No. 6, 1693–1704, 2010.

[18] Zhang, A., J. Xu, and Z. Liu, "An X-band centrosymmetric microstrip bandpass filter with reflectionless range over 3.9-18.6 GHz and stopband up to 40 GHz," *Microwave and Optical Technology Letters*, Vol. 64, No. 1, 10–15, 2022.

[19] Lalbakhsh, A., A. Ghaderi, W. Mohyuddin, R. B. V. B. Simorangkir, N. Bayat-Makou, M. S. Ahmad, G. H. Lee, and K. W. Kim, "A compact c-band bandpass filter with an adjustable dual-band suitable for satellite communication systems," *Electronics*, Vol. 9, No. 7, 1088, 2020.

[20] Najafi, M. and A. R. Hazeri, "Microstrip dual-narrowband bandpass filter with independent passbands," *Wireless Personal Communications*, Vol. 119, 3503–3516, 2021.

[21] Gómez-García, R., L. Yang, J.-M. Muñoz-Ferreras, and D. Psychogiou, "Selectivity-enhancement technique for stepped-impedance-resonator dual-passband filters," *IEEE Microwave and Wireless Components Letters*, Vol. 29, No. 7, 453–455, 2019.

[22] Cao, Y., Y. Fang, X.-M. Luo, Z.-J. Zhu, and S. Ding, "A compact dual-band bandpass filter for 2.4/5.2 GHz WLAN application," *IEICE Electronics Express*, Vol. 16, No. 20, 20 190 553–20 190 553, 2019.

[23] Chang, H., W. Sheng, J. Cui, and J. Lu, "Multilayer dual-band bandpass filter with multiple transmission zeros using discriminating coupling," *IEEE Microwave and Wireless Components Letters*, Vol. 30, No. 7, 645–648, 2020.

[24] Adli, B., R. Mardiati, and Y. Y. Maulana, "Design of microstrip hairpin bandpass filter for X-band radar navigation," in *2018 4th International Conference on Wireless and Telematics (ICWT)*, 1–6, Nusa Dua, Bali, Indonesia, Jul. 2018.